Tailoring Loose Mg^{2+} Solvation Structure by Steric and Competitive Solvent Coordination for Fast-Charging Magnesium Batteries

Yinlin Shen, Kangjie Xu, Zhirong Zhao-Karger, and Xiangyu Zhao*

Magnesium batteries are attracting growing interest as next-generation energy storage technology due to their high safety, cost-effectiveness, and resource abundance. However, their development remains limited by sluggish Mg^{2+} transport kinetics at the electrode/electrolyte interface. Herein, we propose an electrolyte design strategy that modulates the Mg^{2+} solvation structure by introducing tetrahydrofuran (THF) as a co-solvent into a borate-based electrolyte, Mg[B(hfip)$_4$] (MBF) in dimethoxyethane (DME). THF, selected from a series of linear and cyclic ethers, has a comparable dielectric constant and donor number to DME, but its cyclic structure introduces steric hindrance that induces competitive coordination with Mg^{2+}. This competition weakens Mg^{2+} − solvent interactions, yielding a more labile solvation structure and enhanced desolvation kinetics. As a result, Mg||Mg cells employing the optimized MBF/1D1T electrolyte (DME: THF = 1:1, v:v) exhibit a significantly reduced Mg plating/stripping overpotential of 120 mV at 10 mA cm^{-2}, compared with 316 mV at 8 mA cm^{-2} with MBF/DME, along with exceptional cycling stability exceeding 1200 h. Furthermore, representative sulfide cathodes such as CuS and VS$_4$ demonstrate faster activation and improved high-rate performance in the presence of MBF/1D1T.

1. Introduction

Magnesium-ion batteries (MIBs) have emerged as promising next-generation alternatives to lithium-ion batteries due to the inherent advantages of magnesium metal anode, including natural abundance, low cost, low reduction potential, high theoretical volumetric capacity, and resistance to dendrite formation under mild conditions.[1–3] Despite these advantages, the development of MIBs has long been hindered by

the lack of suitable high-energy-density cathode materials and compatible electrolytes.[3–5] To overcome this limitation, extensive efforts have been devoted to the design of advanced magnesium storage materials, leading to the development of diverse cathode candidates such as metal oxides,[6–8] chalcogenides,[9–11] polyanionic compounds,[12] and organic materials.[13] Among these, conversion-type metal sulfides have garnered particular attention due to their multiple-electron transfer capabilities, enabling higher theoretical capacities.[9,10,14] However, their practical electrochemical performance remains far from ideal, especially under high-rate conditions. To address this, various modification strategies—such as nanostructuring,[15] hybridization with conductive matrices,[16] interlayer expansion,[17] and heterostructure engineering[18]—have been explored. Although these approaches have helped unlock considerable capacity at low current densities,[19] the performance degradation at high rates continues to pose a critical bottleneck. This issue is rooted in the intrinsically sluggish desolvation kinetics of Mg^{2+} ions at the electrode/electrolyte interface, which significantly impedes efficient ion transport and reversible storage.

Unlike monovalent Li$^+$ ions, Mg^{2+} shares a similar ionic radius but carries twice the charge, resulting in stronger electrostatic interactions with coordinating solvents and a higher energy barrier for desolvation. This slow desolvation process often limits Mg^{2+} insertion in the cathode materials, especially in non-layered or narrowly spaced layered materials. In some electrolyte systems, such as fluoroborate-based electrolytes, solvated complexes like [Mg(DME)$_3$]$^{2+}$ bypass desolvation and directly co-intercalate into layered cathodes (e.g., MoS$_2$),[11,20] accelerating reaction kinetics. However, the incorporation of bulky solvated ions can cause structural collapse and limit the generality of this approach. Therefore, for non-layered or high-capacity conversion-type cathodes, efficient Mg^{2+} desolvation at the cathode/electrolyte interface is essential to govern their practical performance.

Growing understanding of solvation structures has spurred considerable interest in electrolyte design for multivalent ion batteries, such as Zn^{2+}, Mg^{2+}, and Ca^{2+} systems.[21–25] Strategies such as introducing strong-coordinating additives or solvents,[26,27] employing bulky cations, or using highly coordinating anions have been proven effective in stabilizing solvated Zn^{2+} structures and suppressing water decomposition at the electrode interface in aqueous zinc-ion batteries.[28,29]

Dr. Y. Shen, K. Xu, Prof. X. Zhao
State Key Laboratory of Materials-Oriented Chemical Engineering, Jiangsu Collaborative Innovation Center for Advanced Inorganic Functional Composites, College of Materials Science and Engineering, Nanjing Tech University, Nanjing 211816, China
E-mail: xiangyu.zhao@njtech.edu.cn
Dr. Z. Zhao-Karger
Helmholtz Institute Ulm (HIU), Electrochemical Energy Storage, Helmholtzstrasse 11, 89081, Ulm, Germany
Institute of Nanotechnology (INT), Karlsruhe Institute of Technology (KIT), Hermann-von-Helmholtz Platz 1, 76344, Eggenstein-Leopoldshafen, Germany
The ORCID identification number(s) for the author(s) of this article can be found under https://doi.org/10.1002/eem2.70124.

In magnesium systems, the introduction of chelating agents like methoxyethylamine has been shown to facilitate a rearrangement of the solvation sheath,[30] enabling Mg^{2+} to bypass the high-energy desolvation step and promoting efficient storage in metal oxides. Similarly, employing strong-coordinating solvents and dissociative calcium salts has enabled solvent-dominated solvation structures,[31] suppressing anion decomposition and allowing reversible calcium plating. Incorporating triflate anions into Mg^{2+} solvation structures can also weaken Mg^{2+}–solvent interactions,[32] lower the desolvation energy barrier, and dramatically enhance Mg storage performance in metal sulfide cathodes, delivering higher capacities, superior rate performance, and faster activation processes. Therefore, the rational design of electrolyte systems, particularly through modulation of solvation structures, presents a simple yet effective strategy for improving the electrochemical kinetics of magnesium metal batteries.

In this work, we develop a solvation engineering strategy by screening linear and cyclic ether solvents for their Mg^{2+} coordination capability, ultimately selecting tetrahydrofuran (THF) as the optimal co-solvent to reconstruct the Mg^{2+} coordination environment in a dimethoxyethane (DME)-based fluoroborate electrolyte ($Mg[B(hfip)_4]_2$/DME). Owing to its similar dielectric constant and donor number, THF competes effectively with DME for Mg^{2+} coordination. Additionally, the steric hindrance of cyclic THF weakens the binding strength of DME, resulting in a more flexible solvation shell and accelerated desolvation kinetics. Spectroscopic analyses, including Fourier-transform infrared (FT-IR) spectroscopy, Raman spectroscopy, and ^{17}O nuclear magnetic resonance (NMR) spectroscopy, combined with density functional theory (DFT) calculations, confirm the weakened Mg^{2+}–solvent interactions in the DME/THF mixed-solvent system. Electrochemical evaluations of Mg‖Cu, Mg‖Mg, and Mg‖sulfide cells demonstrate that employing the optimized $Mg[B(hfip)_4]_2$-based electrolyte with a DME/THF volumetric ratio of 1:1 (MBF/1D1T) enables the cells to achieve significantly enhanced cycling stability and high-rate performance. This competitive coordination strategy offers a practical and generalizable pathway for tailoring solvation structures in multivalent ion electrolytes.

2. Results and Discussion

2.1. Electrolyte Design Principle

In the MBF-based electrolyte, the weak interaction between the Mg ion and the boron-centered anion arises from the high degree of electron delocalization in the borate anion. This characteristic ensures efficient salt dissociation in a variety of organic solvents and results in a low concentration of contact ion pairs, thereby promoting fast Mg^{2+} transport. Moreover, weakened Mg^{2+}–anion interactions allows strong coordination between Mg^{2+} and solvent molecules, exemplified by DME—a widely used solvent in magnesium batteries due to its good compatibility with magnesium anode. Specifically, each Mg^{2+} ion is coordinated by six oxygen atoms from three DME molecules ($[Mg(DME)_3]^{2+}$), with an average Mg–O bond length of 2.094 Å, as confirmed by DFT calculations (**Figure 1a**) and the result of ^1H NMR (Figure S1, Supporting Information). However, this rigid solvation configuration imposes a high-energy barrier to Mg^{2+} desolvation at the electrode/electrolyte interface, thereby severely restricting Mg^{2+} insertion kinetics.

To overcome this limitation, solvent engineering—either by substituting the primary solvent or introducing a co-solvent—offers a

viable strategy. Figure S2, Supporting Information compares the physical properties of linear ethers (dimethoxyethane, DME; diglyme, G2; triglyme, G3; tetraglyme, G4; ethylene glycol diethyl ether, EGDE; diethylene glycol diethyl ether, DEE) and cyclic ethers (tetrahydrofuran, THF; 2-Methyltetrahydrofuran, MeTHF; tetrahydropyran, THP; 1,3-dioxolane, DOL). Linear ethers generally exhibit higher boiling points and lower melting points than cyclic ethers, along with elevated dielectric constants. By contrast, cyclic ethers are characterized by lower dielectric constants, yet their distinct steric hindrance (enhanced Mg–O bond length; Figure 1a) and solvation characteristics may facilitate faster Mg^{2+} desolvation.

When the cyclic ether of THF is used as the sole solvent, Mg^{2+} ions form a six-coordinate structure ($[Mg(THF)_6]^{2+}$, Figure S1, Supporting Information) with an elongated Mg–O bond length of 2.116 Å, attributed to the steric hindrance of the cyclic THF ligands. This configuration results in a looser solvation shell compared with the $[Mg(DME)_3]^{2+}$. Notably, THF and DME exhibit comparable dielectric constants (7.6 vs 7.2) and identical donor numbers (DN = 20), creating a competitive coordination environment in their mixed-solvent systems. Such competition weakens solvent–Mg^{2+} interactions, leading to an overall looser solvation structure. Consequently, Mg^{2+} can undergo desolvation more readily at the electrode interface, thereby enhancing electrochemical kinetics.

Electrostatic potential (ESP, Figure 1b) analysis revealed that in linear ethers such as DME, oxygen atoms exhibit high electron density, facilitating strong coordination with Mg^{2+} ions. However, as the ether chain length increases (e.g., from DME to G2 and G3), electron density becomes more delocalized, weakening Mg^{2+}–solvent interactions.[33] Among cyclic ethers, the five-membered-ring THF exhibits comparable electron enrichment around oxygen atoms, whereas six-membered THP and methyl-substituted MeTHF lack distinct electron-rich regions, indicating lower Mg^{2+} binding affinity. To disrupt the compact solvation structure of $[Mg(DME)_3]^{2+}$, introducing a co-solvent with balanced dielectric properties and steric effects is essential. THF was selected as the optimal co-solvent due to its comparable dielectric constant and DN to DME, coupled with enhanced steric hindrance and electron-rich oxygen atoms that promote a looser Mg^{2+} solvation shell.

A series of single-solvent electrolytes were prepared using 0.3 M MBF salt in DME, G2, G3, THF, THP, and MeTHF. Owing to the presence of weakly coordinating anions, all solvents successfully dissolved the MBF salt (Figure S3, Supporting Information). When tested in Mg‖Cu cells (Figure S4, Supporting Information), all electrolytes—except MBF/THP—exhibited clear Mg plating/stripping behavior under cyclic voltammetry (CV) at scan rates ranging from 1 to 50 mV s^{-1}. Notably, cells employing MBF/DME and MBF/THF electrolytes exhibited significantly enhanced current responses (~26 mA cm^{-2}) compared with other systems (G2: 8 mA cm^{-2}, G3: 2 mA cm^{-2}, MeTHF or THP: <1 mA cm^{-2}), reflecting their superior electrochemical activity. Furthermore, the MBF/DME system demonstrated markedly improved reaction kinetics over MBF/THF, as evidenced by a 198 mV reduction in oxidation peak potential at 50 mV s^{-1}, which correlated with reduced electrochemical polarization.

Figures S5–S7, Supporting Information show the galvanostatic plating/stripping profiles at 1.0 mA cm^{-2} for 10 min, further demonstrating the electrochemical performance of these electrolytes. The low electrochemical polarization of the MBF/DME system aligns with CV observations. Among the tested systems, the MBF/THF system exhibited the highest cycling stability and coulombic efficiency (CE), maintaining an average CE of 99.5% after 500 cycles, followed by
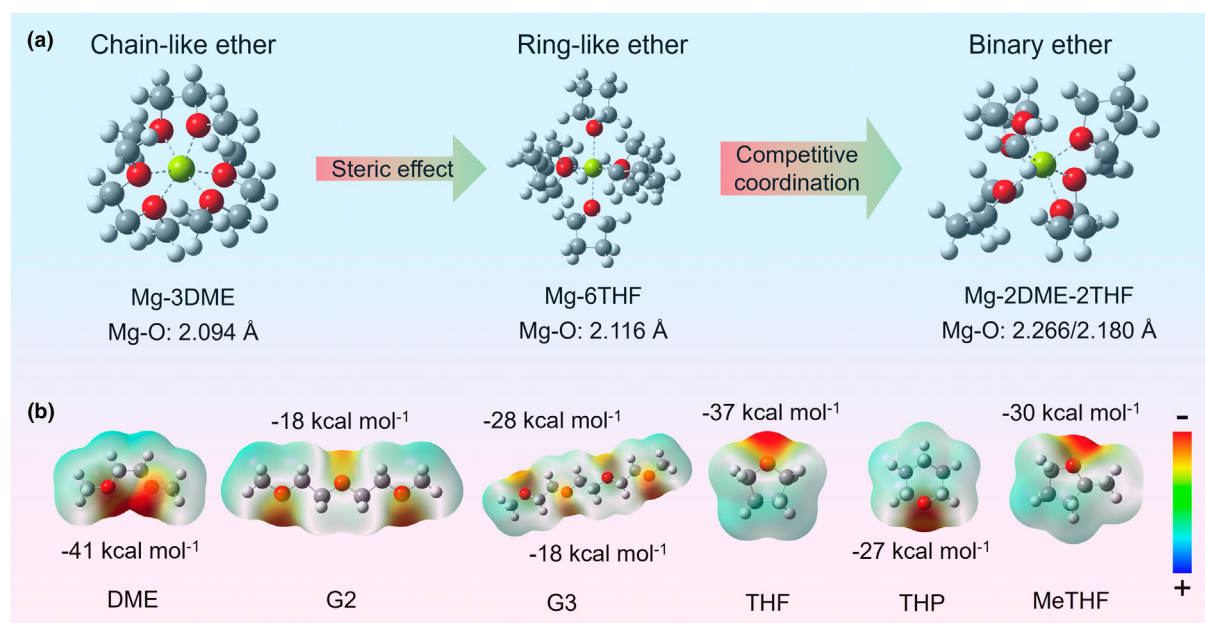
Figure 1. a) Mg^{2+} solvation structure optimized by DFT and b) surface electrostatic potentials of DME, G2, G3, THF, THP, and MeTHF molecules.

MBF/DME (89.1%). Long-term cycling under enhanced areal capacity (1.0 mA cm^{-2}, 1.0 mAh cm^{-2}) further demonstrated the superiority of MBF/THF, achieving an average CE of 98.6% over 200 cycles (Figure S8b, Supporting Information), whereas MBF/DME showed severe degradation (CE of 81.4% after 150 cycles, **Figure 2b**). To evaluate the rate capability of the MBF/THF system (Figure S8c, Supporting Information), deposition current densities were further increased to 2.0, 5.0, and 10.0 mA cm^{-2}. The corresponding overpotentials for magnesium plating on copper were 82, 201, and 323 mV, respectively. These results validate the high compatibility of MBF/THF with magnesium metal anode and its potential for high-rate applications.

2.2. Compatibility of Electrolytes with Mg Metal

To further optimize the Mg^{2+} solvation structure and construct an expanded solvation structure, a series of binary-solvent systems were formulated (Figure 2 and Figures S9 and S10, Supporting Information), including DME + THF, DME + G2, DME + G3, THF + G2, and THF + G3. Among these, the MBF/DME + THF electrolyte (MBF/1D1T) exhibited the best electrochemical performance in Mg‖Cu cells. Long-term deposition/stripping cycling at 1.0 mA cm^{-2} with a deposition capacity of 0.17 mAh cm^{-2} revealed that MBF/1D1T achieved superior stability, the highest CE (>99.5%), and the lowest overpotential (70 mV) among all binary-solvent combinations.

When tested at 1.0 mA cm^{-2} with a higher areal capacity of 1.0 mAh cm^{-2} (Figure 2a), MBF/1D1T delivered an ultra-low Mg plating overpotential of 38 mV. After an initial three-cycle activation process, the CE rapidly stabilized at ~100% (Figure 2b), whereas MBF/DME showed poor cycling stability, with a continuous decline in CE after 80 cycles.

The rate performance of MBF/1D1T was further evaluated by depositing 0.5 mAh cm^{-2} of Mg at various current densities (Figure 2c). The resulting overpotentials were 38, 54, 105, 131, and 136 mV at

0.5, 1.0, 2.0, 5.0, and 10.0 mA cm^{-2}, respectively, indicating excellent compatibility with Mg metal even at high current densities. Moreover, Mg‖Cu cells with MBF/1D1T electrolyte maintained low overpotentials (<250 mV) and high CE (~100%) at elevated areal capacities from 1.0 to 10.0 mAh cm^{-2} (Figure S11, Supporting Information).

Strikingly, in extended cycling tests at a low areal deposition capacity of 0.17 mAh cm^{-2} (1 mA cm^{-2} for 10 min, Figure 2d), the MBF/1D1T-based Mg‖Cu cell maintained stable operation with a high CE of 99.7% for over 900 h (2700 cycles), significantly outperforming the MBF/DME system, which underwent failure after ~200 h (600 cycles). These results underscore the critical role of mixed-solvent strategies in enabling stable and efficient Mg deposition via the formation of favorable solvation structure and electrode/electrolyte interface.

To further investigate the interfacial stability of magnesium metal anodes, Mg‖Mg symmetric cells were assembled and tested in both MBF/DME and MBF/1D1T electrolytes (**Figure 3**). As shown in Figure 3a, under operation at 0.5 mA cm^{-2} with an areal capacity of 0.5 mAh cm^{-2}, the Mg‖Mg symmetric cell using the MBF/1D1T electrolyte exhibited an ultra-low overpotential—only ~16% of that observed in the MBF/DME system—and remained stable over an extended cycling period of 1200 h.

When the current density was further increased (Figure 3b), the Mg‖Mg symmetric cell using MBF/DME showed significant polarization growth and eventually failed at 9.0 mA cm^{-2} due to severe interfacial degradation. By contrast, the Mg‖Mg cell using MBF/1D1T maintained low overpotentials up to 10 mA cm^{-2}, demonstrating superior rate capability and interfacial stability. Specifically, the MBF/1D1T system exhibited overpotentials of 66 mV (1.0 mA cm^{-2}), 71 mV (2.0 mA cm^{-2}), 73 mV (5.0 mA cm^{-2}), 118 mV (8.0 mA cm^{-2}), and 120 mV (10.0 mA cm^{-2}), with negligible increments (<2%) between 8.0 and 10.0 mA cm^{-2} (Figure 3c). Conversely, the MBF/DME system showed significantly higher overpotentials of 120 mV (1.0 mA cm^{-2}), 148 mV (2.0 mA cm^{-2}), 197 mV
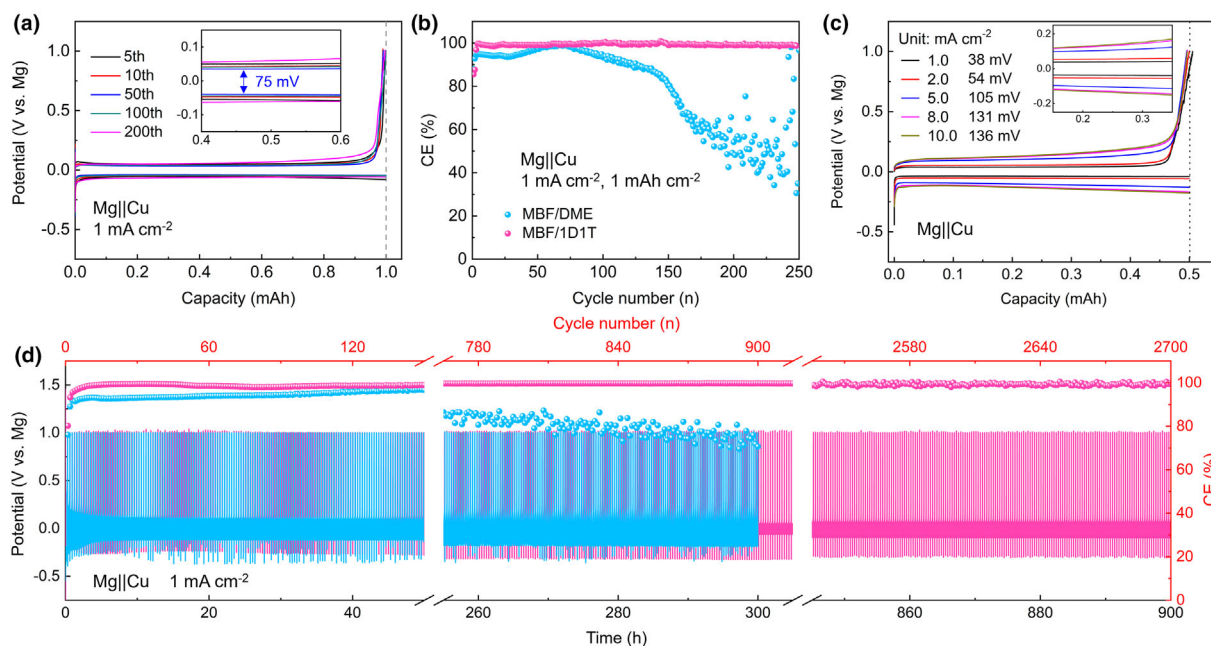
Figure 2. a) Voltage profiles and b) CE of Mg‖Cu asymmetric cells using the MBF/DME or MBF/1D1T electrolyte at 1 mA cm^{-2} and 1 mAh cm^{-2}. c) Voltage profiles of a Mg‖Cu asymmetric cell using the MBF/1D1T electrolyte at current densities ranging from 1 to 10 mA cm^{-2}. d) Cycling performance of Mg‖Cu asymmetric cells using the MBF/DME or MBF/1D1T electrolyte at 1 mA cm^{-2}.
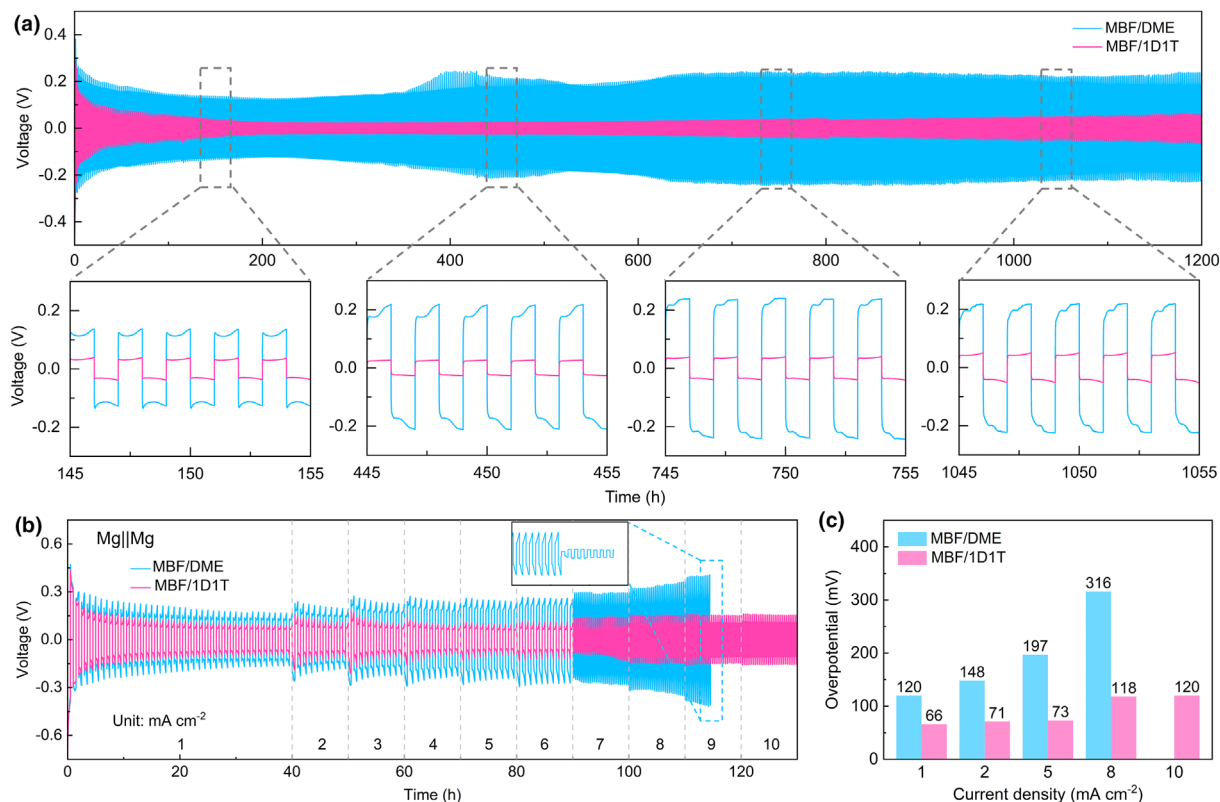

Figure 3. a) Voltage profiles of Mg‖Mg symmetric cells at 0.5 mA cm^{-2} with 0.5 mAh cm^{-2} using MBF/DME and MBF/1D1T electrolytes. b) Rate performance and c) corresponding overpotentials of Mg‖Mg symmetric cells using MBF/DME and MBF/1D1T electrolytes.
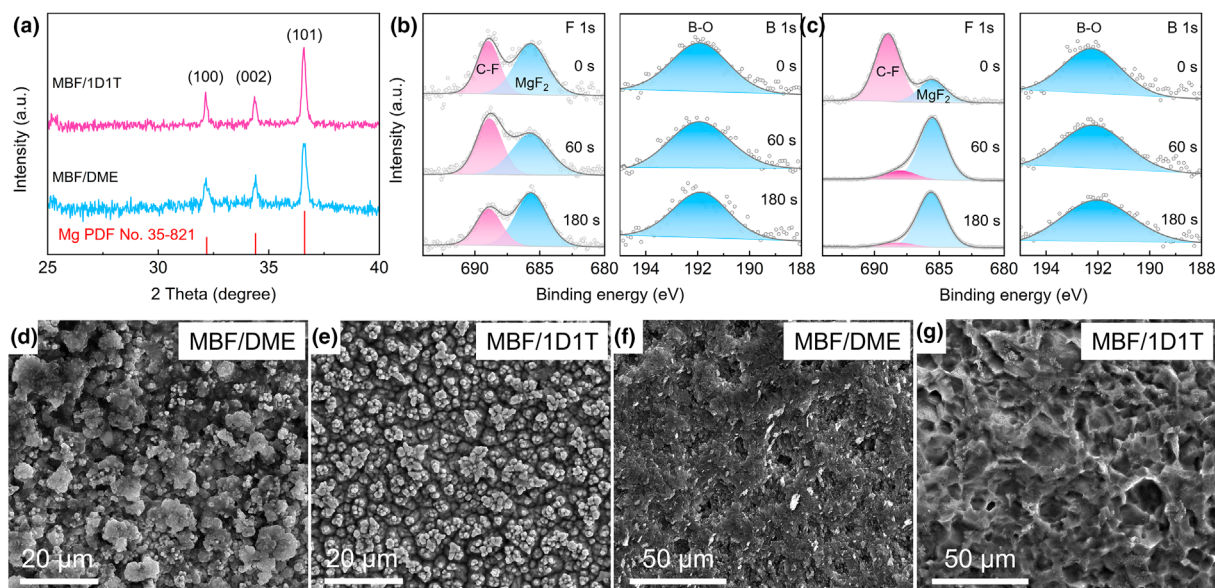
Figure 4. a) XRD patterns of Mg deposits on Cu foils in MBF/DME and MBF/1D1T. XPS spectra (F 1s and B 1s) and SEM images of Mg deposits on Cu foils in b, d) MBF/DME and c, e) MBF/1D1T. SEM images of Mg metal surface after 50 cycles in f) MBF/DME and g) MBF/1D1T.

$(5.0~\mathrm{mA~cm^{-2}})$, and 316 mV $(8.0~\mathrm{mA~cm^{-2}})$, accompanied by large voltage fluctuations beyond $5.0~\mathrm{mA~cm^{-2}}$. Moreover, the MBF/DME system could not sustain stable operation at $5~\mathrm{mA~cm^{-2}}$ without a prior activation process involving several tens of cycles at lower current densities $(0.5~\mathrm{and}~1~\mathrm{mA~cm^{-2}})$. By contrast, the MBF/1D1T system enabled stable cycling over 400 h at $5~\mathrm{mA~cm^{-2}}$ (areal capacity: 2.5 mAh $\mathrm{cm^{-2}}$), maintaining consistently low polarization throughout the test (Figure S12, Supporting Information).

The ultra-low overpotentials observed in both Mg‖Cu and Mg‖Mg cells using MBF/1D1T highlight fast $\mathrm{Mg^{2+}}$ desolvation and efficient charge transfer at the electrode/electrolyte interface. The introduction of THF has been shown to enhance the ionic conductivity of the Mg-ion electrolyte $(11.07~\mathrm{mS~cm^{-1}}$ for MBF/DME and 13.48 mS $\mathrm{cm^{-1}}$ for MBF/1D1T). Furthermore, the exceptionally long-term cycling stability confirms the excellent compatibility of the MBF/1D1T electrolyte and magnesium metal anodes, positioning it as a promising electrolyte for high-performance Mg batteries.

Desolvation behavior at the anode/electrolyte interface plays a crucial role in determining Mg deposition characteristics. X-ray diffraction (XRD), X-ray photoelectron spectroscopy (XPS), and scanning electron microscopy (SEM) analyses (**Figure 4**) were performed on magnesium deposits $(5~\mathrm{mAh~cm^{-2}}$ on copper foil) and cycled magnesium foils. Figure 4a shows the XRD patterns of magnesium deposits in the MBF/1D1T and MBF/DME electrolytes, where only copper (PDF card no. 4-836) and Mg [(100), (002), and (101) lattice planes; PDF card no. 35-821] diffraction peaks are observed, indicating high-purity Mg deposition without detectable impurities. In the MBF/DME electrolyte, the Mg deposits exhibit comparable diffraction peak intensities for the (100) and (002) planes, suggesting that the growth rates of metallic Mg along the (100) and (001) crystallographic directions are nearly identical. By contrast, Mg deposited from the MBF/1D1T electrolyte shows a stronger (100) peak relative to (002) peak, indicating preferential growth along the (100) direction. This orientation change implies that the introduction of THF suppresses Mg growth along the

(001) axis, likely due to the preferential adsorption of THF molecules on the (002) surface of metallic Mg.[34]

The composition and structure of the surface layer formed on the deposited Mg were investigated via XPS depth profiling (Figure 4b,c, and Figure S13, Supporting Information). Both the MBF/DME and MBF/1D1T electrolytes yielded Mg deposits containing Mg, B, F, and C elements, indicating the formation of F- and B-rich solid electrolyte interface (SEI) layers. Detailed analysis of F 1s and B 1s region spectra revealed that, in the MBF/DME system, surface fluorine species predominantly consisted of organic C−F (688.9 eV) and inorganic $\mathrm{MgF_2}$ (685.7 eV). As the etching depth increased, the proportion of organic components decreased, but even after 180 s of etching, organic species remained prevalent, indicating the coexistence of organic and inorganic components throughout the interfacial layer. By contrast, for magnesium deposited from the MBF/1D1T electrolyte, organic species (likely from residual electrolyte salts) were detected on the surface but diminished rapidly with etching depth, ultimately revealing a $\mathrm{MgF_2}$-dominated inorganic SEI layer that is beneficial for $\mathrm{Mg^{2+}}$ conduction.

To further elucidate the chemical composition of the SEI, additional XPS analyses were conducted for C 1s, O 1s, and Mg 1s regions (Figure S13, Supporting Information). The C 1s spectra show characteristic peaks of C−C, C−O, and C=O bonds, attributed to solvent (DME or THF) decomposition, along with a C−F peak originating from anion decomposition. Prior to sputtering, stronger C−F signals were observed on Mg deposited from the MBF/1D1T electrolyte, indicating the presence of fluorinated organic species on the surface. However, these signals declined sharply after 60 s of etching, whereas in the MBF/DME system, C−F signals remained persistent—consistent with the trend observed in the F 1s region—further confirming a more organic-rich SEI in the MBF/DME electrolyte.

The O 1s spectra may include contributions from adsorbed oxygen (due to air exposure), $\mathrm{MgO/Mg(OH)_2}$, C−O/C=O functional groups, and B−O bonds. However, accurate deconvolution of the O 1s region is complicated by signal overlap and the potential for fitting bias. Given
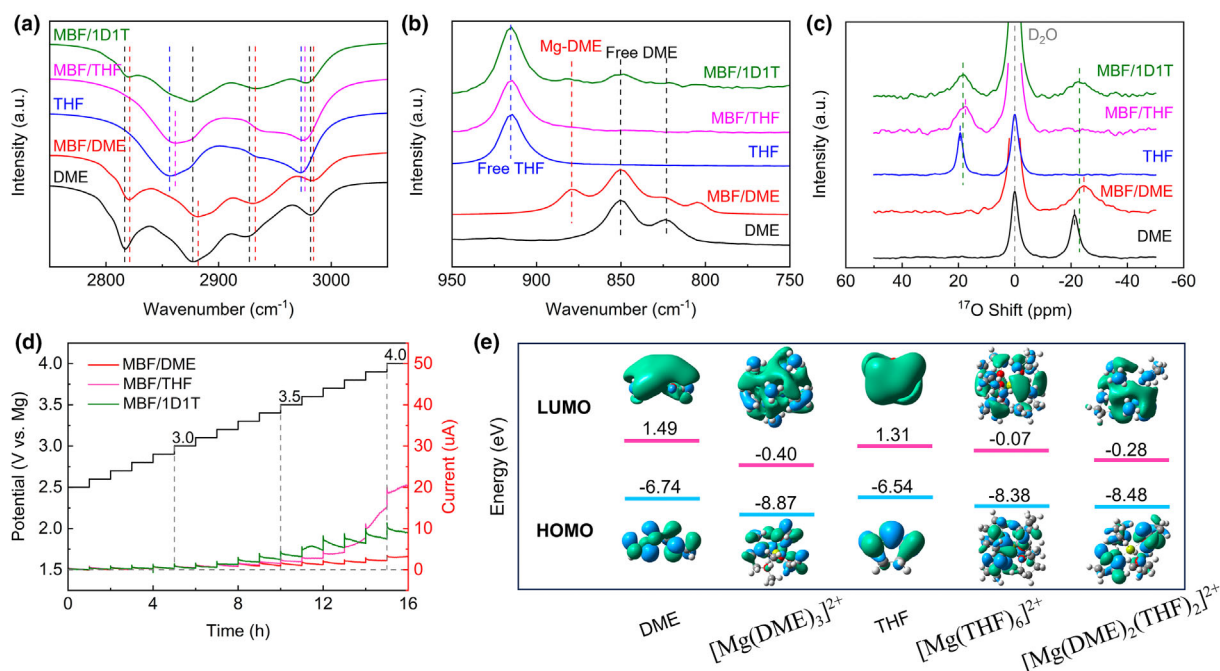
Figure 5. a) FT-IR spectra, b) Raman spectra, and c) ^{17}O NMR data of different solvents and electrolytes. d) Chronoamperometry curves of Mg∥Al cells using different electrolytes measured from 2.5 to 4.0 V versus Mg. e) Calculated HOMO and LUMO energy levels of DME, THF, and solvated Mg-ions ([Mg(DME)$_3$]$^{2+}$, [Mg(THF)$_6$]$^{2+}$, and [Mg(DME)$_2$(THF)$_2$]$^{2+}$).

these limitations, the existing depth-resolved XPS data for Mg, C, B, and F elements are considered sufficient to characterize the interfacial chemistry and evaluate SEI composition. Collectively, the results demonstrate that the MBF/1D1T electrolyte favors the formation of a thinner, more inorganic, and MgF$_2$-rich SEI, while the MBF/DME electrolyte leads to a thicker, more organic-containing interphase, which may contribute to inferior interfacial stability and Mg deposition behavior.

The morphology of deposited magnesium on copper foil was examined. In the MBF/DME electrolyte (Figure 4d and Figure S14a,b, Supporting Information), the deposits exhibited particle sizes ranging from tens of nanometers to several micrometers. Conversely, deposition from MBF/1D1T yielded a smoother surface composed of uniformly stacked ~1 μm particles (Figure 4e and Figure S14c,d, Supporting Information). The low polarization, stable long-term cycling, and excellent rate performance of the Mg∥Cu cell can be attributed to the uniform magnesium deposition morphology. After multiple cycles, the Mg foil in MBF/DME showed a pitted surface (Figure 4f and Figure S15a, Supporting Information), indicative of locally electrochemical activity with passivated regions, whereas the cycled magnesium foil in MBF/1D1T exhibited a uniform 3D network structure (Figure 4g and Figure S15b, Supporting Information), indicating full surface utilization, which greatly improves long-term stability and activation behavior.

2.3. Mg^{2+} Solvation Structure

The interaction between Mg^{2+} and solvent molecules was systematically investigated using FT-IR, Raman spectroscopy, and ^{17}O NMR

(Figure 5). These techniques provide complementary insights into the solvation behavior of Mg^{2+} in single- and binary-solvent systems. In the FT-IR spectra (Figure 5a), characteristic peaks at 2816, 2877, 2927, and 2981 cm^{-1} corresponded to vibrational modes of free DME molecules. Upon addition of 0.3 M magnesium salt, these peaks shifted to higher wavenumbers (2821, 2881, 2932, and 2984 cm^{-1}), indicating coordination between oxygen atoms of DME and Mg^{2+} ions. Similarly, for THF, the free solvent peaks at 2856 and 2973 cm^{-1} also shifted to higher wavenumbers (2861 and 2977 cm^{-1}) upon Mg-salt addition. Notably, in the MBF/1D1T binary-solvent system, the IR peaks were at 2819, 2877, 2932, and 2981 cm^{-1}. The peak shifts for both DME and THF were significantly smaller compared to their respective single-solvent systems, suggesting weaker Mg^{2+}–solvent interactions in the mixed electrolyte. This weaker interaction implies that solvent molecules can more easily dissociate from the solvation shell during electrochemical processes. The Raman spectra in Figure 5b exhibited a similar trend to the FT-IR results, further confirming that solvation interactions between Mg^{2+} and solvent molecules are reduced in the binary-solvent electrolyte. This observation aligns with a loosely coordinated solvation structure, which facilitates faster desolvation kinetics.

To gain deeper insight into the Mg–O coordination environment, ^{17}O NMR spectroscopy was performed using D$_2$O as an external reference. For pristine DME, the oxygen atom showed a chemical shift at −21.3 ppm. In the MBF/DME electrolyte, a downfield shift to −24.7 ppm was observed, indicating coordination between DME and Mg^{2+}. A similar shift (from 19.4 to 17.7 ppm) was observed for THF in the MBF/THF electrolyte. Notably, in the MBF/1D1T binary-solvent electrolyte, the chemical shift changes for both DME (−23.0 ppm) and
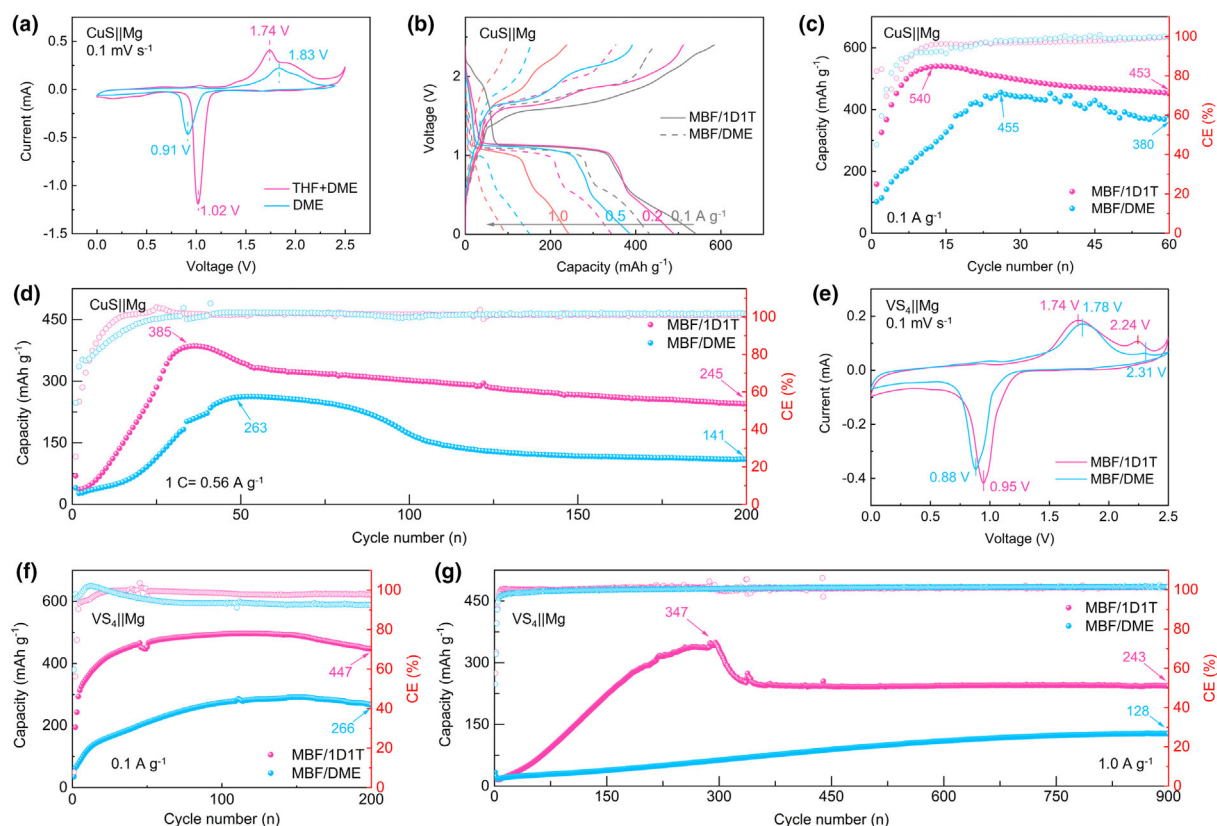
Figure 6. a) CV curves at 0.1 mV s^{-1}, b) charge/discharge profiles at different current densities, and cycling performance at c) 0.1 A g^{-1} and d) 0.56 A g^{-1} of Mg‖CuS cells in the MBF/DME and MBF/1D1T electrolytes. e) CV curves 0.1 mV s^{-1} of Mg‖VS$_4$ cells using MBF/DME and MBF/1D1T electrolytes. Cycling performance of Mg‖VS$_4$ cells at f) 0.1 A g^{-1} and g) 0.56 A g^{-1} using MBF/DME and MBF/1D1T electrolytes.

THF (18.5 ppm) were smaller than those in their single-solvent counterparts, suggesting that competitive solvent coordination weakens individual solvent−Mg^{2+} interactions. This weakened solvation interaction facilitates fast Mg^{2+} desolvation, enabling highly reversible Mg plating/stripping in both Mg‖Cu and Mg‖Mg cells even under ultrahigh current densities. To determine whether the solvents also participate in anion coordination, the electrolytes were dried to isolate recrystallized magnesium salts, which were then characterized by ^{11}B and ^{17}F NMR spectroscopy (Figure S16, Supporting Information). The chemical shifts of both boron and fluorine in the recrystallized salts showed negligible deviations from those in pristine MBF, indicating that neither DME nor THF coordinates with the anion. These results confirm that the addition of THF modifies only the cationic solvation structure, without affecting the coordination environment of the anions.

Chronoamperometry measurements of Mg‖Al cells (Figure 5d) revealed that all three electrolytes exhibited anodic stability above 3.5 V, indicating good compatibility with high-voltage cathodes. This is notable because DME and THF are typically unsuitable for high-voltage applications due to oxidative instability. However, Mg^{2+} coordination alters the solvents' electronic environment: The highest occupied molecular orbital (HOMO) energy levels of the solvated solvent molecules are significantly lowered by strong electrostatic interaction with Mg^{2+}, suppressing solvent oxidation and extending the electrolyte's anodic stability. These results highlight the critical role of Mg^{2+}-induced solvation effects in stabilizing ether-based electrolytes.

2.4. Electrochemical Performance of Mg‖Sulfide Cells

To verify the compatibility of the MBF/1D1T electrolyte with cathode materials, transition metal sulfides, specifically CuS and VS$_4$ (high theoretical capacity sulfides), were tested. **Figure 6** compares the electrochemical performance of the CuS cathode in MBF/DME and MBF/1D1T. CV curves (Figure 6a) showed distinct redox peaks corresponding to the Cu^{2+}/Cu^0 redox pair in both electrolytes. Notably, the peak currents were significantly higher, and the voltage gap between redox peaks decreased from 0.92 to 0.72 V of the CuS cathode in MBF/1D1T, indicating improved kinetics. The CuS cathode in MBF/1D1T also exhibited an activation process (Figure S17, Supporting Information), attributed to nanostructuring of the electrode material.

To further highlight the improved kinetics of the cathode material in the mixed electrolyte, the CuS cathode was subjected to charge/discharge tests at different current densities (Figure 6b). As the current density increased, the CuS cathode delivered discharge capacities of 445/540, 349/488, 162/386, and 108/247 mAh g^{-1} in MBF/DME and MBF/1D1T, respectively, at 0.1, 0.2, 0.5, and 1.0 A g^{-1}. Compared with MBF/DME, the CuS cathode in the mixed electrolyte exhibited 1.2, 1.4, 2.4, and 2.3 times higher capacities, indicating that the rapid desolvation in MBF/1D1T provides enhanced performance advantages at high-rate conditions.

Furthermore, the Mg‖CuS cells in the MBF/1D1T electrolyte showed reduced charge/discharge polarization, with clear charge/discharge

plateaus maintained even at a high current density of 1.0 A g^{-1}. The cells cycled at 0.1 A g^{-1} (Figure 6c) and 0.56 A g^{-1} (Figure 6d) exhibited activation behavior consistent with CV observations. Notably, activation proceeded significantly faster in MBF/1D1T than in MBF/DME. At 0.1 A g^{-1}, the CuS cathode in MBF/1D1T achieved a maximum capacity of 540 mAh g^{-1} (96.4% of its theoretical value) by the 13th cycle, surpassing 455 mAh g^{-1} of the cathode in MBF/DME after 30 cycles. The Mg‖CuS battery cycled in MBF/1D1T maintained a capacity of 453 mAh g^{-1} after 60 cycles, which is higher than the 380 mAh g^{-1} achieved in MBF/DME. Even at a higher current density of 0.56 A g^{-1}, MBF/1D1T enabled faster activation, higher reversible capacity, and enhanced capacity retention (245 mAh g^{-1} versus 141 mAh g^{-1} in MBF/DME after 200 cycles) of the CuS cathode. The improved electrochemical properties of the Mg‖CuS cell using the MBF/1D1T electrolyte stem from fast desolvation kinetics, accelerated interfacial charge transfer, and stable magnesium plating/stripping.

Another tested sulfide cathode material is VS$_4$, whose phase structure, thermogravimetric analysis, XPS results, and morphological characteristics are provided in Figures S18 and S19, Supporting Information. The CV curves of Mg‖VS$_4$ cells in both electrolytes showed distinct redox peaks (Figure 6e). Notably, the cell using MBF/1D1T exhibited smaller electrochemical polarization, indicating enhanced reaction kinetics. In addition, the VS$_4$ cathode demonstrated a pronounced electrochemical activation process in the MBF/1D1T electrolyte (Figure S20, Supporting Information).

Further insights into the activation behavior are provided by the cycling performance at 0.1 A g^{-1} (Figure 6f). The VS$_4$ cathode in MBF/1D1Tdelivered an initial discharge capacity of 34 mAh g^{-1} but underwent rapid activation, reaching over 450 mAh g^{-1} by the 36th cycle. By contrast, the same electrode in MBF/DME only achieved 291 mAh g^{-1}. After 200 cycles, the discharge capacity remained at 447 mAh g^{-1} in MBF/1D1T, whereas it dropped to 266 mAh g^{-1} in MBF/DME. At a higher current density of 1.0 A g^{-1} (Figure 6g), both systems exhibited similar initial discharge capacities and activation trends. In MBF/1D1T, the VS$_4$ cathode reached a maximum capacity of 347 mAh g^{-1} at the 350th cycle and retained 243 mAh g^{-1} after 900 cycles. By contrast, the cathode in MBF/DME remained in an activation phase throughout 900 cycles, ending with a final capacity of 128 mAh g^{-1}, approximately half of that achieved in MBF/1D1T. These results collectively demonstrate the superior electrochemical performance of VS$_4$ in MBF/1D1T, characterized by high reversible capacity, good rate capability, and long-term cycling stability.

3. Conclusion

In summary, a mixed-solvent electrolyte strategy was developed by incorporating THF—an ether solvent with dielectric constant and donor number comparable with DME—into the MBF/DME electrolyte. The sterically hindered THF molecules competitively coordinated with Mg^{2+}, thereby weakening the overall Mg–solvent interaction. Comprehensive spectroscopic characterizations, including Raman, FT-IR, and ^{17}O NMR, confirmed the formation of a weakly coordinated solvation structure in the tailored MBF/1D1T electrolyte. This optimized solvation environment led to significantly improved interfacial properties with magnesium metal, as evidenced by an ultra-low deposition overpotential of 38 mV at 1 mA cm^{-2}, which is significantly lower than 179 mV observed in MBF/DME electrolyte, and only 136 mV at 10 mA cm^{-2}. Furthermore, Mg‖Cu and Mg‖Mg cells employing

MBF/1D1T demonstrated remarkable cycling stability, operating steadily for 900 and 1200 h, respectively, surpassing the 200 and 300 h achieved with the MBF/DME counterpart. Furthermore, the MBF/1D1F electrolyte enabled markedly more uniform Mg deposition compared with MBF/DME, indicating improved interfacial stability. When applied to sulfide-based cathode materials, MBF/1D1T enabled shortened activation processes and improved rate performance. Notably, the CuS and VS$_4$ cathodes exhibited approximately 2.3- and 2.7-fold higher capacity at 1.0 A g^{-1}, respectively, compared to those paired with MBF/DME. These findings highlight the effective competitive coordination strategy in modulating multivalent Mg^{2+} solvation structures.

4. Experimental Section

Materials: Di-n-butyl magnesium (Mg(Bu)$_2$, 1 M heptane solution), 1,1,1,3,3,3-hexafluoro-2-propanol (HFIP-H), and borane tetrahydrofuran complex solution (BH$_3$-THF) were purchased from Macklin and used without further purification. DME (Macklin, 99.9%), G2 (Macklin, 99.5%), G3 (Macklin, 99.9%), THF (Aladdin, 99.9%), MeTHF (Aladdin, 99.5%), and THP (Aladdin, 99.9%) were used after being dehydrated with a 4-Å molecular sieve.

Electrolytes preparation: 2.13 mL HFIP-H was dissolved in 5 mL DME in a 100 mL glass bottle, and then 10 mL 1 M Mg(Bu)$_2$/heptane solution was added slowly and stirred for 5 h. At the same time, 7.07 mL HFIP-H was dissolved in 5 mL DME in a 20 mL glass bottle, and then 24.4 mL BH$_3$-THF solution was slowly added and stirred for 5 h. After that, the above solutions were mixed together and stirred at RT for 12 h. Finally, the Mg[B(hfip)$_4$]$_2$ salt was obtained by vacuum heating at 60 °C for 24 h. The magnesium salts were dissolved in single or binary ether solvents in a volumetric flask to obtain electrolytes of specific concentrations. The concentration of electrolytes is 0.3 M.

Synthesis of CuS and VS$_4$ materials: CuS material was synthesized following a previous report.[10] VS$_4$ material was synthesized through a hydrothermal method using vanadium ammonium (NH$_4$VO$_3$) as the vanadium source, thioacetamide as the sulfur source, graphite oxide (GO) as the carrier, and deionized water as the solvent. Generally, 144 mg of GO was ultrasonically dispersed in 80 mL of deionized water for 2 h. Then, 1.06 g of NH$_4$VO$_3$ and 6.85 g of thioacetamide were added to the dispersion and stirred magnetically for 2 h. The mixture was transferred to a 100 mL Teflon-lined autoclave and heated at 160 °C for 24 h. The black product was washed several times with water and ethanol. Finally, the product was dried in a vacuum oven at 80 °C for 12 h.

Material characterization: XRD was conducted on a Rigaku SmartLab instrument (Cu-Kα, λ = 1.5418 Å, 9 kW). SEM (ZEISS GeminiSEM 300) and XPS (Thermo Scientific Nexsa) were applied to analyze the samples' morphology and composition. Raman (WITec alpha 300R) and FT-IR (PerkinElmer) were used to characterize the electrolytes' solvation structure. The instrument used for ^{17}O NMR test was Bruker 300 MHz. To avoid the influence of deuterated reagents on the solvation structure, the ^{17}O NMR test used coaxial nuclear magnetic tubes and the deuterated reagent was deuteroxide.

Electrode preparation: The CuS or VS$_4$ electrodes were prepared by coating 60 wt.% active materials, 30 wt.% carbon black, and 10 wt.% polyvinylidene fluoride onto copper foil. This assembly was subsequently dried overnight in a vacuum at 80 °C. The resulting mass loading is about 2 mg cm^{-2}.

Electrochemical measurements: The cells were assembled in 2032 coin-type cells in an Ar-filled glove box. Glass fiber (Whatman GF/F) was used as the separator, and polished magnesium metal (50 μm thick) functioned as the counter electrode. Galvanostatic tests were conducted using the Neware battery test system (CT-4008T) and the LAND battery test system (CT2001A). CV data were collected using a potentiostat (VMP3, Bio-Logic) electrochemical workstation. All electrochemical tests were conducted at 298 K. The specific capacities were calculated based on the mass of CuS or VS$_4$ material in the cathode.

Quantum chemistry calculations: The quantum chemistry calculations were performed using the ORCA package employing the resolution of identity approximation.[35] All the DFT calculations were performed using the PBE functional. Basis sets of def2-TZVP[36,37] were adopted for all atoms in the complexes

with decontracted auxiliary def2-TZVP/J Coulomb fitting basis sets.[38] D3 dispersion correction developed by Grimme is included for weak interactions.[39] Visualization of ESP is made by using GaussView6.0 software.

Conflict of Interest

The authors declare no conflict of interest.

Supporting Information

Supporting Information is available from the Wiley Online Library or from the author.

Keywords

[1] R. Mohtadi, O. Tutusaus, T. S. Arthur, Z. Zhao-Karger, M. Fichtner, *Joule* **2021**, *5*, 581.
[2] D. Chen, X. Ren, T. Li, Z. Chen, Y. Cao, F. Xu, *Energy Environ. Mater.* **2023**, *6*, e12486.
[3] P. Bonnick, J. Muldoon, *Adv. Funct. Mater.* **2020**, *30*, 1910510.
[4] F. Liu, T. Wang, X. Liu, L.-Z. Fan, *Adv. Energy Mater.* **2021**, *11*, 2000787.
[5] Y. Pang, Z. Nie, F. Xu, L. Sun, J. Yang, D. Sun, F. Fang, S. Zheng, *Energy Environ. Mater.* **2024**, *7*, e12527.
[6] T. Koketsu, J. Ma, B. J. Morgan, M. Body, C. Legein, W. Dachraoui, M. Giannini, A. Demortiere, M. Salanne, F. Dardoize, *Nat. Mater.* **2017**, *16*, 1142.
[7] J. L. Andrews, A. Mukherjee, H. D. Yoo, A. Parija, P. M. Marley, S. Fakra, D. Prendergast, J. Cabana, R. F. Klie, S. Banerjee, *Chem* **2018**, *4*, 564.
[8] L. Thanh Son, T. H. Hoa, D. Q. Truong, *J. Electroanal. Chem.* **2019**, *848*, 113293.
[9] Y. Shen, Q. Zhang, Y. Wang, L. Gu, X. Zhao, X. Shen, *Adv. Mater.* **2021**, *33*, 2103881.
[10] Y. Shen, Y. Wang, Y. Miao, M. Yang, X. Zhao, X. Shen, *Adv. Mater.* **2020**, *32*, 1905524.
[11] Z. Li, X. Mu, Z. Zhao-Karger, T. Diemant, R. J. Behm, C. Kubel, M. Fichtner, *Nat. Commun.* **2018**, *9*, 5115.
[12] Y. Zhang, J. Gui, T. Li, Z. Chen, S.-a. Cao, F. Xu, *Chem. Eng. J.* **2020**, *399*, 125689.
[13] H. Dong, O. Tutusaus, Y. Liang, Y. Zhang, Z. Lebens-Higgins, W. Yang, R. Mohtadi, Y. Yao, *Nat. Energy* **2020**, *5*, 1043.
[14] X. Zhou, J. Tian, J. Hu, C. Li, *Adv. Mater.* **2018**, *30*, 1704166.
[15] V. Duffort, X. Sun, L. F. Nazar, *Chem. Commun.* **2016**, *52*, 12458.
[16] H. Tian, T. Gao, X. Li, X. Wang, C. Luo, X. Fan, C. Yang, L. Suo, Z. Ma, W. Han, *Nat. Commun.* **2017**, *8*, 14083.
[17] Y. Xu, X. Deng, Q. Li, G. Zhang, F. Xiong, S. Tan, Q. Wei, J. Lu, J. Li, Q. An, *Chem* **2019**, *5*, 1194.
[18] L. Zhou, F. Xiong, S. Tan, Q. An, Z. Wang, W. Yang, Z. Tao, Y. Yao, J. Chen, L. Mai, *Nano Energy* **2018**, *54*, 360.
[19] M. Mao, T. Gao, S. Hou, F. Wang, J. Chen, Z. Wei, X. Fan, X. Ji, J. Ma, C. Wang, *Nano Lett.* **2019**, *19*, 6665.
[20] H. D. Yoo, Y. L. Liang, H. Dong, J. H. Lin, H. Wang, Y. S. Liu, L. Ma, T. P. Wu, Y. F. Li, Q. Ru, *Nat. Commun.* **2017**, *8*, 339.
[21] H. Cheng, Q. Sun, L. Li, Y. Zou, Y. Wang, T. Cai, F. Zhao, G. Liu, Z. Ma, W. Wahyudi, *ACS Energy Lett.* **2022**, *7*, 490.
[22] H. Fan, X. Zhang, J. Xiao, W. Chen, Q. Lin, Z. S. Ng, Y. Lin, Y. Su, L. Pan, Y. Su, S. Ren, H. Liu, X. Li, Y. Zhang, *Energy Environ. Mater.* **2024**, *7*, e12792.
[23] J. Cao, Y. Liu, K. Li, I. Zatovsky, J. Yang, H. Liu, Z. Gu, X. Gao, K. Zhang, S. Zheng, X. Wu, *Natl. Sci. Rev.* **2025**, *12*, nwaf074.
[24] G. Li, K. Chen, M. Lei, T. Wang, M. Hu, C. Li, *Adv. Energy Mater.* **2024**, *14*, 2401507.
[25] M. Hu, G. Li, K. Chen, X. Zhou, C. Li, *Chem. Eng. J.* **2024**, *480*, 148193.
[26] Y. Xu, G. Zhou, S. Zhao, W. Li, F. Shi, J. Li, J. Feng, Y. Zhao, Y. Wu, J. Guo, *Adv. Sci.* **2019**, *6*, 1800981.
[27] X. Li, T. Gao, F. Han, Z. Ma, X. Fan, S. Hou, N. Eidson, W. Li, C. Wang, *Adv. Energy Mater.* **2018**, *8*, 1701728.
[28] Y. Shi, Y. Chen, L. Shi, K. Wang, B. Wang, L. Li, Y. Ma, Y. Li, Z. Sun, W. Ali, *Small* **2020**, *16*, 2000730.
[29] H. Ren, S. Li, B. Wang, Y. Zhang, T. Wang, Q. Lv, X. Zhang, L. Wang, X. Han, F. Jin, *Adv. Mater.* **2023**, *35*, e2208237.
[30] S. Hou, X. Ji, K. Gaskell, P.-F. Wang, L. Wang, J. Xu, R. Sun, O. Borodin, C. Wang, *Science* **2021**, *374*, 172.
[31] Z. Hou, R. Zhou, Y. Yao, Z. Min, Z. Lu, Y. Zhu, J. M. Tarascon, B. Zhang, *Angew. Chem. Int. Ed.* **2022**, *61*, e202214796.
[32] Y. Shen, Y. Wang, Y. Miao, Q. Li, X. Zhao, X. Shen, *Adv. Mater.* **2023**, *35*, e2208289.
[33] X. Li, M. Zhao, Y. Song, C. Bi, Z. Li, Z. Chen, X. Zhang, B. Li, J. Huang, *Chem. Soc. Rev.* **2025**, *54*, 4822.
[34] Y. Sun, Y. Wang, L. Jiang, D. Dong, W. Wang, J. Fan, Y. Lu, *Energy Environ. Sci.* **2023**, *16*, 265.
[35] F. Neese, *WIREs Comput. Mol. Sci.* **2011**, *2*, 73.
[36] A. Schäfer, *J. Chem. Phys.* **1994**, *100*, 5829.
[37] F. Weigend, *Chem. Phys. Lett.* **1998**, *294*, 143.
[38] F. Weigend, *Phys. Chem. Chem. Phys.* **2006**, *8*, 1057.
[39] S. Grimme, *J. Chem. Phys.* **2010**, *132*, 154104.